Nanoscale

PAPER

View Article Online
View Journal | View Issue

Cite this: *Nanoscale*, 2015, **7**, 1224

Defective TiO_2-supported Cu nanoparticles as efficient and stable electrocatalysts for oxygen reduction in alkaline media†

Ke Liu, Yang Song and Shaowei Chen*

Received 17th October 2014,
Accepted 21st November 2014

DOI: 10.1039/c4nr06128d

www.rsc.org/nanoscale

Nanocomposites based on TiO_2-supported copper nanoparticles were prepared by a hydrothermal method where copper nanoparticles with or without the passivation of 1-decyne were chemically grown onto TiO_2 nanocolloid surfaces (and hence denoted as CuHC10/TiO_2 and Cu/TiO_2, respectively). Transmission electron microscopy measurements showed that the size of the hybrid nanoparticles was 5–15 nm in diameter with clearly defined lattice fringes for anatase TiO_2(101) and Cu(111). The formation of anatase TiO_2 nanoparticles was also observed by X-ray diffraction measurements. FTIR measurements confirmed successful attachment of alkyne ligands onto the surface of the copper nanoparticles *via* Cu–C≡ interfacial bonds in CuHC10/TiO_2. XPS measurements suggested the formation of CuO in both samples with a higher concentration in Cu/TiO_2, and interestingly Ti^{3+} species were found in CuHC10/TiO_2 but were absent in Cu/TiO_2 or TiO_2 nanoparticles. Electrochemical studies demonstrated that both Cu/TiO_2 and CuHC10/TiO_2 exhibited a markedly improved electrocatalytic performance in the oxygen reduction reaction, as compared to TiO_2 nanocolloids alone, in the context of the onset potential, the number of electrons transferred and the kinetic current density. Importantly, among the series, CuHC10/TiO_2 exhibited the best ORR activity with a high current density, an almost four-electron reduction pathway and long-term stability after 4000 cycles at high potentials, which may be ascribed to the defective TiO_2 structures in combination with surface ligand engineering.

1. Introduction

Proton exchange membrane fuel cells (PEMFC) are clean, efficient and environmentally friendly electrochemical power generators.[1] However, the sluggish kinetics of the oxygen reduction reaction (ORR) at the cathode represents one of the greatest challenges in the widespread commercialization of PEMFC. Carbon-supported platinum-based nanoparticle catalysts have been extensively used for fuel cell electrodes,[2–4] yet further improvement of their performance is urgently needed due to the scarcity and high cost of platinum. In fact, a variety of strategies have been developed to improve the ORR activities, such as preparation of Pt-based alloys[5] and surface functionalization of Pt nanoparticles with selected organic ligands.[6–8] An alternative approach is to replace Pt with earth-abundant non-precious materials.[9] Among these, little attention has been paid to copper-based electrocatalysts although copper is inexpensive and abundant with remarkable conductivity.[10–12] In fact, copper has been used extensively as supporting or non-active components in the oxygen reduction reactions,[13–15] although ORR activities of poly- or single-crystalline bulk copper have been reported in the literature in a borax buffer solution[16,17] or in a sulfuric acid solution.[18] More recently, it has been shown that the ORR activity might be markedly enhanced with alkyne-capped nanosized copper particles,[19] suggesting that copper, when properly engineered, might be a viable material for ORR electrocatalysis.

Note that metal nanoparticle catalysts are usually dispersed on substrates of high surface areas and/or good conductivity. Of these, carbon black is one of the most commonly used catalyst supports in the oxygen reduction reaction due to its high surface area and good electronic conductivity.[20,21] However, oxidation of carbon supports at potentials higher than +0.9 V *vs.* RHE causes degradation in the catalyst performance during fuel cell operation.[22] Therefore, it is important to identify oxidation-resistant catalyst supports to meet the durability requirements of PEMFC catalysts. Titanium dioxide has been regarded as an attractive support for ORR catalysts due to its low cost, abundance, and long-term chemical stability under extreme conditions. In addition, the hypo-d-electron nature of titanium dioxide enables strong metal–support

Department of Chemistry and Biochemistry, University of California, 1156 High Street, Santa Cruz, California 95064, USA. E-mail: shaowei@ucsc.edu

†Electronic supplementary information (ESI) available: FTIR spectra and Koutecky–Levich plots. See DOI: 10.1039/c4nr06128d

interactions,[23,24] leading to an enhanced dispersion of catalyst nanoparticles and improved catalytic activities. In fact, it has been reported that platinum nanoparticles supported on TiO_2 nanoparticles possess a greater surface area[25] and a higher ORR activity than commercial Pt/C,[26] and PtPd/TiO_2 nanocomposite electrocatalysts showed an activity comparable to that of Pt/C with enhanced stability at high potentials.[27] Therefore, TiO_2 appears to be a promising alternative for a ORR catalyst support.[28] This is the primary motivation for the present study where we examine the ORR activity of nanocomposites based on copper nanoparticles supported on TiO_2 nanocolloids.

Herein anatase TiO_2 nanocolloids were prepared by the hydrolysis of titanium(IV) *n*-butoxide with the assistance of chloroaniline and oleic acid *via* hydrothermal treatment. Then copper nanoparticles were chemically grown on TiO_2 nanocolloids by simple sodium borohydride reduction, as manifested by TEM and XRD measurements. FTIR measurements confirmed the successful attachment of the alkyne ligands onto the nanoparticle surface in CuHC10/TiO_2 possibly by the formation of Cu–C≡ interfacial bonds. XPS measurements revealed that CuO species were formed in the nanocomposites, with a concentration higher in Cu/TiO_2 than in CuHC10/TiO_2. Interestingly, Ti(III) species were identified in CuHC10/TiO_2 but were absent in Cu/TiO_2, which was believed to be beneficial to the electronic conductivity of the TiO_2 supports.[29] Electrochemical studies indicated that the oxygen reduction reaction proceeded mainly *via* the 4e pathway on both Cu/TiO_2 and CuHC10/TiO_2 samples as compared to the 2e pathway on TiO_2 nanoparticles alone. Excellent long-term stability was also retained for the nanocomposite catalysts after 4000 cycles at high potentials, and CuHC10/TiO_2 samples stood out as the best catalysts among the series, which is likely the combined results of defective support and surface ligand engineering.

2. Experimental section

2.1. Chemicals

3-Chloroaniline (99%, ACROS), titanium(IV) *n*-butoxide (99%, ACROS), oleic acid (Fisher Scientific), Nafion® 117 solution (Fluka), copper acetate ($Cu(OAc)_2{\cdot}H_2O$, 99.9%, Alfa Aesar), 1-decyne (HC10, TCI America), and sodium borohydride ($NaBH_4$, ≥98%, ACROS) were all used as received. Solvents were purchased at the highest purity available from typical commercial sources and also used without further treatment. Water was deionized with a Barnstead Nanopure water system (18.3 MΩ cm). Ultrapure N_2 and O_2 were used for the deaeration of the electrolyte solutions and oxygen reduction reactions, respectively.

2.2. Preparation of TiO_2 supported Cu nanoparticles

TiO_2 nanoparticles were prepared by following a literature procedure.[30] In a typical reaction, 0.05 mL of 3-chloroaniline was added to 5 mL of Nanopure water and then transferred to a Teflon-lined stainless-steel autoclave. Meanwhile, 0.085 g of titanium(IV) *n*-butoxide and 0.5 mL of oleic acid were dissolved in 5 mL of toluene and also transferred to the autoclave. The mixed solution was subjected to hydrothermal treatment at 180 °C for 12 h, and the as-obtained white precipitates (TiO_2) were collected and rinsed extensively with methanol.

The TiO_2 nanoparticles prepared above were then used for the preparation of Cu–TiO_2 nanocomposites. In a typical reaction, a calculated amount of copper acetate and TiO_2 nanoparticles (at a TiO_2 : Cu molar ratio of 4 : 1) was dispersed in THF. $NaBH_4$ dissolved in a small amount of water was added dropwise under vigorous stirring and N_2 protection, where the color of the solution was found to change quickly from blue to dark brown, signifying the formation of copper nanoparticles. After one hour of magnetic stirring, the solution was dried and the solids were washed with a copious amount of methanol to remove reaction byproducts or excess ligands, affording purified nanocomposites that were denoted as Cu/TiO_2.

CuHC10/TiO_2 was prepared in a similar fashion except that a 10-fold molar excess of 1-decyne was added to the solution prior to the addition of $NaBH_4$.

2.3. Characterization

The morphology and sizes of the nanoparticles were characterized by transmission electron microscopy studies (TEM, Philips CM300 at 300 kV). X-ray diffraction (XRD) measurements were performed with a Rigaku Miniflex powder diffractometer using Cu Kα radiation with a Ni filter (λ = 0.154059 nm at 30 kV and 15 mA) which features a detection limit of 0.04°. X-ray photoelectron spectra (XPS) were recorded with a PHI 5400/XPS instrument equipped with an Al Kα source operated at 350 W and 10^{-9} Torr. Silicon wafers were sputtered with argon ions to remove carbon from the background and used as substrates. The Si 2p peak (99.15 eV) was used as the reference, and deconvolution of the XPS spectra was carried out by using XPSPEAK 4.1.

2.4 Electrochemistry

Electrochemical tests were carried out in a standard three-electrode cell connected to a CHI 710C electrochemical workstation, with a Pt foil counter electrode and a Hg/HgO (0.1 M NaOH aq.) reference electrode. The working electrode is a rotating (platinum) ring-(glassy-carbon) disk electrode (RRDE). To prepare catalyst solutions for oxygen reduction tests, typically 0.4 mg of the nanocomposite catalysts and 1.6 mg of carbon black with 4 μL of Nafion were ultrasonically mixed in 0.4 mL of ethanol. Then 15 μL of the catalyst ink was slowly dropcast onto the glassy-carbon disk electrode of the RRDE and dried under gentle N_2 (corresponding to a loading of 15 μg in total including TiO_2 and copper nanoparticles). When the electrode was dried, a dilute Nafion solution (0.1 wt%, 3 μL) was added onto it, prior to being immersed into electrolyte solutions for electrochemical measurements.

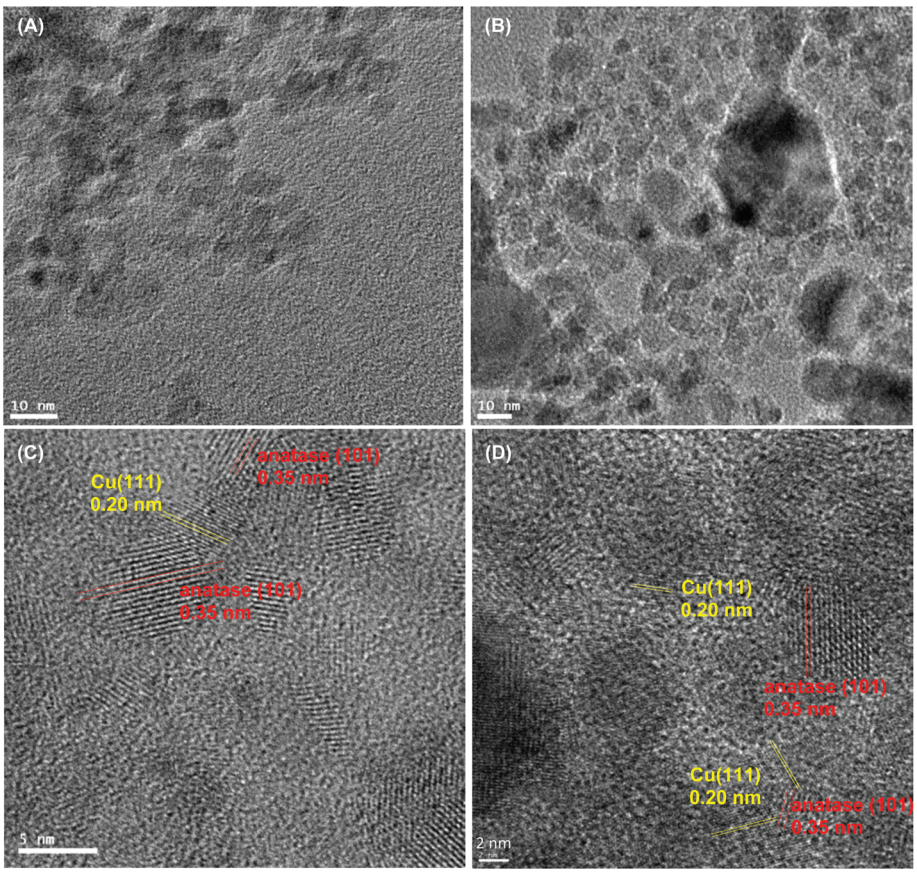

Fig. 1 Representative TEM micrographs of (A and C) Cu/TiO_2 and (B and D) $CuHC10/TiO_2$ nanoparticles. Scale bars are 10 nm in panels (A) and (B), 5 nm in (C) and 2 nm in (D). Yellow lines highlight the Cu(111) lattice fringes whereas red lines are for anatase TiO_2 (101).

3. Results and discussion

Fig. 1 shows the representative TEM micrographs of the (A) Cu/TiO_2 and (B) $CuHC10/TiO_2$ nanoparticles. In both images, individual nanoparticles can be identified but with rather apparent agglomeration, especially the Cu/TiO_2 samples in panel (A), and the size of the hybrid nanoparticles ranges from 5 to 15 nm in diameter. High-resolution imaging in panels (C) and (D) shows that indeed copper nanoparticles were grown on TiO_2 nanocolloid surfaces, forming nanocomposites, as manifested by the well-defined lattice fringes for Cu(111) and anatase TiO_2(101) that were in intimate contact and featured an interlayer spacing of 0.20 and 0.35 nm, respectively.[31,32] In addition, the Cu nanocrystals were observed to be around 2 nm whereas TiO_2 was markedly larger at 5 nm and above.

The structures of the nanocomposites were then characterized by XRD measurements. Fig. 2 shows the XRD patterns of the TiO_2 (black curve), Cu/TiO_2 (red curve) and $CuHC10/TiO_2$ (green curve) nanoparticles, all of which exhibited a series of diffraction peaks (labelled as @) at 25.3°, 37.9°, 48.0°, 54.5° and 62.8°, corresponding to the (101), (004), (200), (213), and (116) crystalline planes of anatase TiO_2 (JCPDS 75-1537), respectively. Furthermore, based on the width of these diffraction peaks, the average size (τ) of the TiO_2 nanocrystallites may be quantitatively estimated by using the Debye–Scherrer equation, $\tau = K\lambda/\beta\cos\theta$, where K is a dimensionless shape

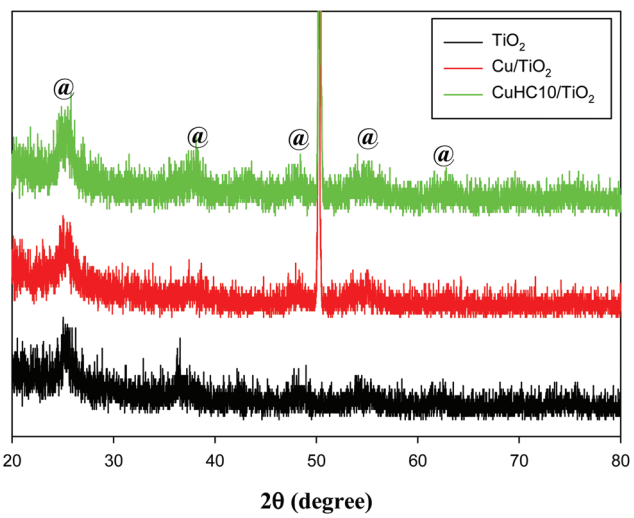

Fig. 2 XRD patterns of TiO_2 (black curve), Cu/TiO_2 (red curve) and $CuHC10/TiO_2$ (green curve) nanoparticles. Legends "@" highlight the diffraction peaks of anatase TiO_2.

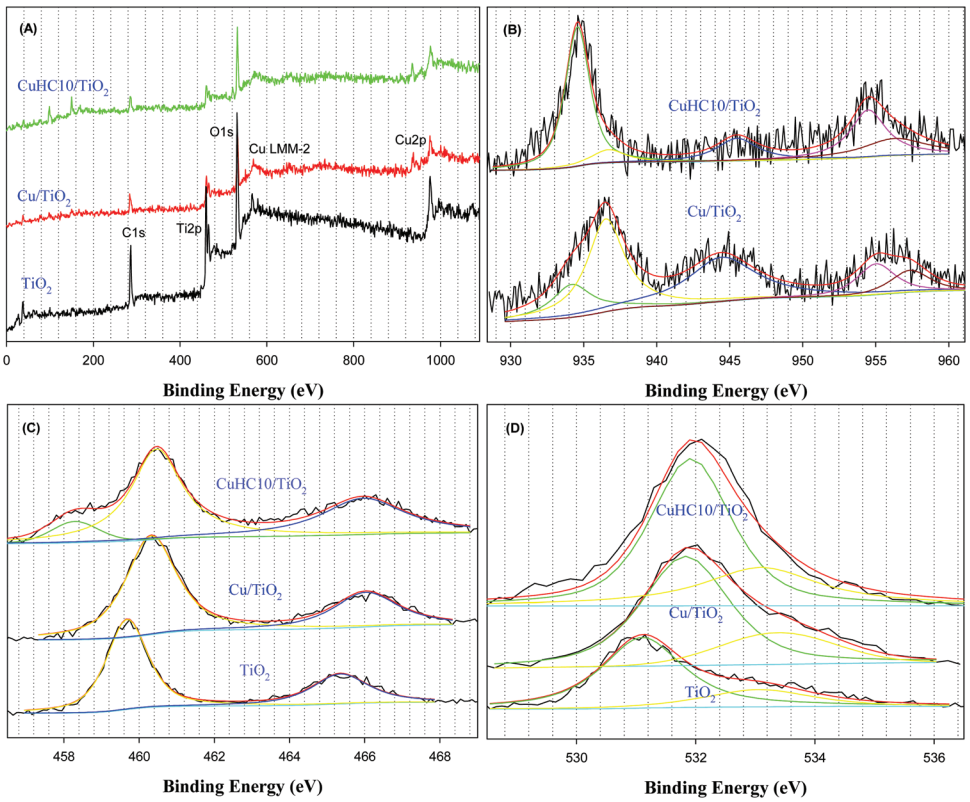

Fig. 3 XPS full survey spectra (A) and high-resolution scans of the (B) Cu 2p, (C) Ti 2p and (D) O 1s electrons of TiO_2, Cu/TiO_2 and $CuHC10/TiO_2$ nanoparticles. Black curves show experimental data and color curves show deconvolution fits.

factor with a value of 0.9, λ is the X-ray wavelength (1.54059 Å for Cu Kα), and β is the full width at half-maximum (fwhm) of a selected diffraction peak. On the basis of the TiO_2(101) peaks, the size (τ) was quantified and actually very consistent among the three samples, 5.1 nm for the as-prepared TiO_2, 4.1 nm for Cu/TiO_2, and 5.5 nm for $CuHC10/TiO_2$, which is in good agreement with the TEM results presented in Fig. 1. Note that no Cu diffraction patterns can be identified by XRD measurements, probably because of the small size and low loading of the Cu nanocrystals‡ (Fig. 1).

The successful passivation of the copper nanoparticles by the decyne ligands in $CuHC10/TiO_2$ is manifested by FTIR measurements, as shown in Fig. S1.† It can be seen that the ≡C–H vibrational stretch at 3312 cm^{-1} and bending vibration at 628 cm^{-1} were well-defined for the monomeric ligands of 1-decyne (red curve); yet both vanished in the case of nanoparticle samples (black curve, where the broad peak centered at 3300 cm^{-1} was likely due to residual water). This suggests that efficient breaking of the ≡C–H bond after the alkyne ligands were adsorbed onto the copper nanoparticle surface. In addition, the absence of this vibration band also indicates that the $CuHC10/TiO_2$ nanocomposites were free of excessive alkyne ligands. In addition the C≡C vibrational stretch can be identified at 2120 cm^{-1} for monomeric 1-decyne ligands, yet this band red-shifted to 1720 cm^{-1} for the $CuHC10/TiO_2$ nanoparticles. This phenomenon may be explained by the cleavage of the ≡C–H bond and the formation of Cu–C≡ interfacial linkages, where the conjugated metal–ligand bonds led to effective intraparticle charge delocalization between the particle-bound acetylene moieties and hence a decreasing bonding order of the C≡C moieties, as observed in previous studies.[8]

The chemical nature of the hybrid nanoparticles was then examined by XPS measurements. Fig. 3(A) shows the full survey spectra of TiO_2, Cu/TiO_2 and $CuHC10/TiO_2$ composite nanoparticles. In TiO_2 nanocolloids, four major peaks can be readily identified at 286 eV (C 1s), 460 eV (Ti 2p), 536 eV (O 1s) and 976 eV (oxygen Auger). For Cu/TiO_2 and $CuHC10/TiO_2$ hybrid nanoparticles, additional peaks emerged, and the peak at *ca.* 935 eV may be ascribed to Cu 2p electrons, whereas the peak at around 570 eV most likely arose from the Cu LMM-2 auger transitions of Cu_2O.[33] This suggests the successful deposition of copper on the TiO_2 surface where cuprous oxide (Cu_2O) likely formed within the nanoparticles. Furthermore, based on the corresponding integrated peak areas, the Cu/Ti atomic ratio was found to be rather consistent between the two hybrid nanoparticles, 14.7% for Cu/TiO_2 and 12.6% for $CuHC10/TiO_2$.

‡Whereas the sharp peak at 50.4° appeared to be consistent with diffraction from the Cu(200) crystalline planes, a much more intense diffraction peak for Cu(111) should have emerged at 43.4°. This was not observed in Fig. 2. Thus it is unlikely that the sharp peak at 50.4° arose from copper nanoparticles. Its origin is unknown at this point.

High-resolution scans of the Cu 2p electrons in Cu/TiO_2 and $CuHC10/TiO_2$ are shown in panel (B), where the black curves show the experimental data and colored curves show deconvolution fits. For both samples deconvolution yields two pairs of doublets for the Cu 2p electrons. For Cu/TiO_2, the first doublet can be identified at 934.3 and 955.1 eV, which might be ascribed to metallic Cu 2p electrons, and the second doublet at 936.8 and 957.5 eV most likely arising from CuO. Similar behaviors can be seen with the $CuHC10/TiO_2$ hybrids, where metallic Cu 2p can be found at 934.6 and 954.5 eV and CuO at 937.1 and 956.4 eV (note that the binding energies of the Cu 2p electrons for Cu(0) and Cu(I) are only 0.1 eV apart, thus the data likely reflected the combined contributions from both species).[34] One can see that the CuO concentration in Cu/TiO_2 was significantly greater than that in $CuHC10/TiO_2$. In fact, based on the integrated peak areas, the ratio of Cu(II) over the entire copper species in the nanoparticles was estimated to be 48.2% for Cu/TiO_2 and 13.0% for $CuHC10/TiO_2$.

The formation of cupric oxide (CuO) in the nanoparticles is also manifested by the satellite peak between the twin peaks.[35] Note that the appearance of the satellite peak has been largely ascribed to the shake-up effect where the outgoing electron interacts with a valence electron and excites it to a higher energy level.[35] Cu(II) components exhibit a vacant 3d orbital while Cu(I) or Cu(0) features a $3d^{10}$ electronic configuration with 4s being the lowest-energy empty orbital. Therefore, one can see from panel (B) that the higher Cu(II) concentration in Cu/TiO_2 nanoparticles is consistent with the satellite peak (943.89 eV) that was somewhat red-shifted as compared to that (944.96 eV) of $CuHC10/TiO_2$ nanoparticles, and the peak intensity of the former is markedly greater than that of the latter, likely because of effective protection of the nanoparticle surface by the decyne ligands in $CuHC10/TiO_2$.

High-resolution scans of the Ti 2p electrons of TiO_2, Cu/TiO_2 and $CuHC10/TiO_2$ are shown in panel (C). All three nanoparticle samples yield a doublet that is consistent with TiO_2 colloids reported previously,[36] 459.7 and 465.4 eV for TiO_2, 460.3 and 466.0 eV for Cu/TiO_2, and 460.5 and 466.0 eV for $CuHC10/TiO_2$. In addition, it is apparent that the $CuHC10/TiO_2$ nanoparticles show an extra peak at a somewhat lower energy (458.2 eV) than that of Ti(IV) (460.5 eV), which might be assigned to Ti(III),[37] and from the integrated peak area the relative ratio of Ti(III) over Ti(IV) was estimated to be 19.8%. In contrast, no Ti(III) was observed in Cu/TiO_2, which was likely due to the high concentration of CuO that impeded the reduction of Ti(IV) to Ti(III).

Panel (D) shows the corresponding high-resolution scans of the O 1s electrons. The O 1s spectra of all three samples can be deconvoluted into a main peak at 531 eV and a shoulder at a higher binding energy of about 533 eV. The main peaks are consistent with those reported in the literature for bulk oxides, and the binding energy of the shoulders is in agreement with that of surface OH species.[38] The relative amounts of surface OH species can be quantified on the basis of the corresponding integrated peak areas: 29.6% for TiO_2, 30.2% for Cu/TiO_2, and 44.1% for $CuHC10/TiO_2$. It has been reported that hydroxyl groups are formed on TiO_2 surfaces during water dissociation with oxygen vacancies as the active sites.[39] In the present study, whereas the concentration of surface oxygen vacancies was rather comparable between TiO_2 and Cu/TiO_2, it was markedly higher in $CuHC10/TiO_2$. This is consistent with the formation of Ti(III) species in the $CuHC10/TiO_2$ nanoparticles as observed above that likely played an important role in enhancing the ORR activity, as detailed below.

Interestingly, both the Cu/TiO_2 and $CuHC10/TiO_2$ nanocomposites synthesized above exhibited apparent electrocatalytic activities towards oxygen reduction in alkaline media. Fig. 4 shows the steady-state cyclic voltammograms of a glassy-carbon electrode (out of a platinum ring-glassy carbon disk electrode) modified with a calculated amount of TiO_2, Cu/TiO_2 and $CuHC10/TiO_2$ in a N_2-saturated 0.1 M NaOH solution. There are several aspects that warrant attention here. First, TiO_2 nanoparticles exhibited only featureless double-layer charging currents (black curve), primarily because of the large bandgap of TiO_2, hence low electronic conductivity within the potential range of +0.1 to +1.1 V.[40] Second, the double-layer charging currents were markedly enhanced when the electrode was modified with Cu/TiO_2 (red curve) or $CuHC10/TiO_2$ (green curve) nanoparticles. For instance, the double-layer charging currents at +0.40 V increased in the order of $1(TiO_2) : 1.35(Cu/TiO_2) : 2.70(CuHC10/TiO_2)$, signifying enhanced dispersion of the hybrid nanoparticles on the electrode surface. Additional contributions might arise from the enhanced conductivity of $CuHC10/TiO_2$ by defective Ti(III) species (Fig. 3).[29] Furthermore, two anodic peaks emerged at around +0.55 V and +0.84 V (*vs.* RHE), where the former might be ascribed to the formation of a monolayer of Cu_2O while the latter might be ascribed to the formation of a thick multilayer film of CuO, and concurrently, a cathodic peak can be seen at around +0.66 V, likely arising from the partial reduction of CuO to Cu_2O.[41] Similar voltammetric features have also been observed in a

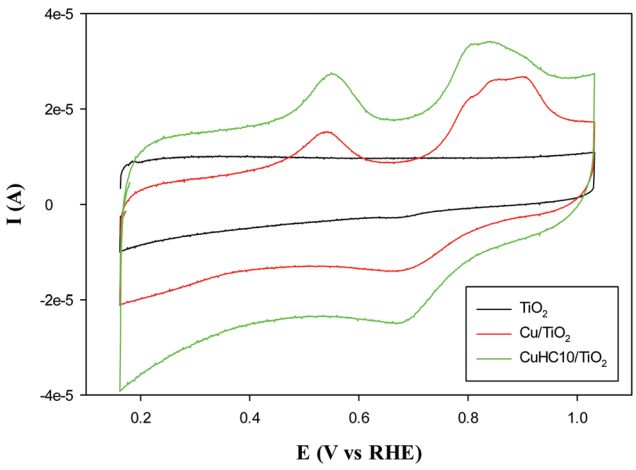

Fig. 4 Cyclic voltammograms of a glassy carbon-disk electrode modified with 15 μg of TiO_2 (black curve), Cu/TiO_2 (red curve) or $CuHC10/TiO_2$ (green curve) nanoparticles in a nitrogen-saturated 0.1 M NaOH solution. Potential scan rate: 10 mV s^{-1}.

previous study with decyne-capped copper nanoparticles.[19] Finally, the fact that these voltammetric peak currents were only slightly greater for CuHC10/TiO_2 than for Cu/TiO_2 suggests that electrochemically accessible surface areas of copper nanoparticles were rather comparable in both hybrid nanoparticles.

Fig. 5 shows the RRDE voltammograms of the same electrodes in an O_2-saturated 0.1 M NaOH solution at different rotation rates. For all three electrodes, it can be seen that significant cathodic currents started to emerge at sufficiently negative potentials indicating an apparent electrocatalytic activity towards oxygen reduction. For (A) TiO_2 and (B) Cu/TiO_2 catalysts, the onset potential was identified at around +0.74 V, and for (C) CuHC10/TiO_2 nanoparticles it was somewhat more positive at +0.75 V. In addition, with the CuHC10/TiO_2 and Cu/TiO_2 nanocomposites the limiting currents were significantly increased, as compared to that of TiO_2 alone. For instance, for TiO_2 nanoparticle catalysts alone, the limiting current at 2500 rpm was only about 0.87 mA, but almost doubled to 1.54 mA with Cu/TiO_2 and to 1.50 mA with CuHC10/TiO_2.

Furthermore, the voltammetric currents collected at the ring electrode, where the potential was set at +1.3 V, were about an order of magnitude lower than the corresponding disk currents, signifying that only a minimal amount of peroxide species was produced during oxygen reduction. From the ratio of the ring current (I_R) and disk current (I_D), the number of electrons transferred (n) during oxygen reduction can be estimated using $n = 4I_D/(I_D + I_R/N)$, with N being the collection efficiency (37%), as shown in Fig. 6. It can be seen that for TiO_2, n increased from zero to 2 rapidly with the electrode potential swept from +0.76 V to +0.70 V, while for Cu/TiO_2 and CuHC10/TiO_2 the increase was much more drastic. At more negative potentials the n values increased accordingly and finally reached 2.69 for TiO_2, 3.74 for Cu/TiO_2 and 3.69 for CuHC10/TiO_2, and the corresponding fractions of peroxide species in the reaction products were estimated to be 65.5%, 13.0% and 15.5%, respectively. It is well known that oxygen reduction in aqueous solutions typically occurs through two major pathways: the direct four-electron reduction pathway from O_2 to OH^- ($n = 4$) and the two-electron reduction pathway from O_2 to H_2O_2 ($n = 2$). This means that at TiO_2 alone, the oxygen reduction was dominated by the 2-electron pathway, while the 4-electron reduction pathway was the dominant one for Cu/TiO_2 and CuHC10/TiO_2.

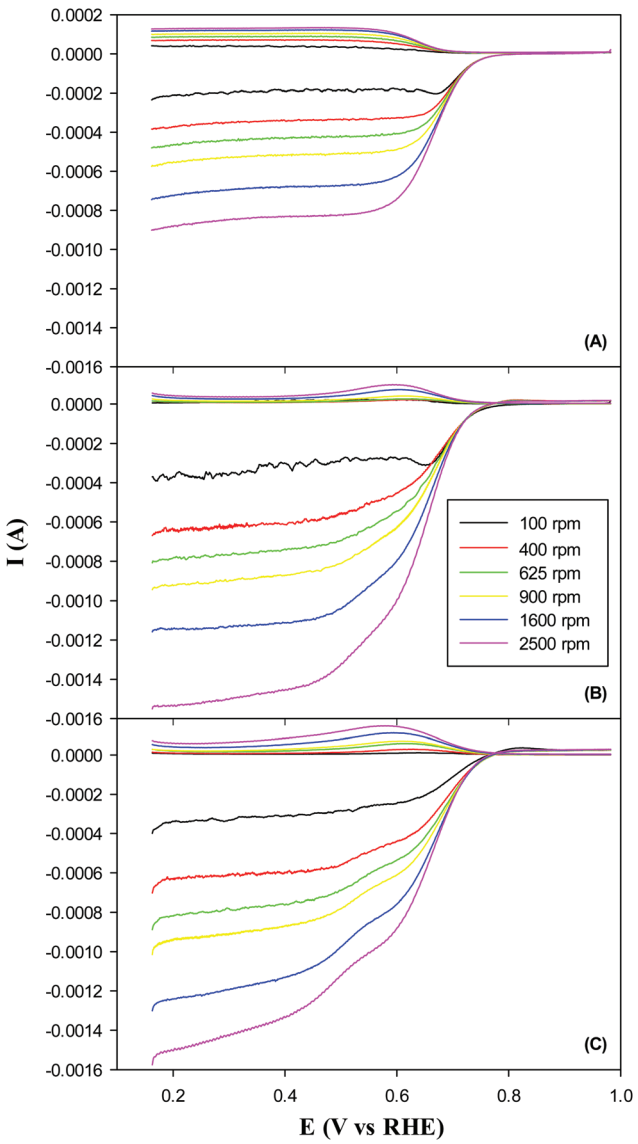

Fig. 5 RRDE voltammograms of a platinum ring-glassy-carbon disk electrode with the disk modified with (A) TiO_2, (B) Cu/TiO_2, and (C) CuHC10/TiO_2 nanoparticles in an oxygen-saturated 0.1 M NaOH solution. Nanoparticle loading is 15 μg. Electrode rotation rates are specified in the figure legends. Ring currents are collected by setting the ring potential at +1.3 V *vs.* RHE.

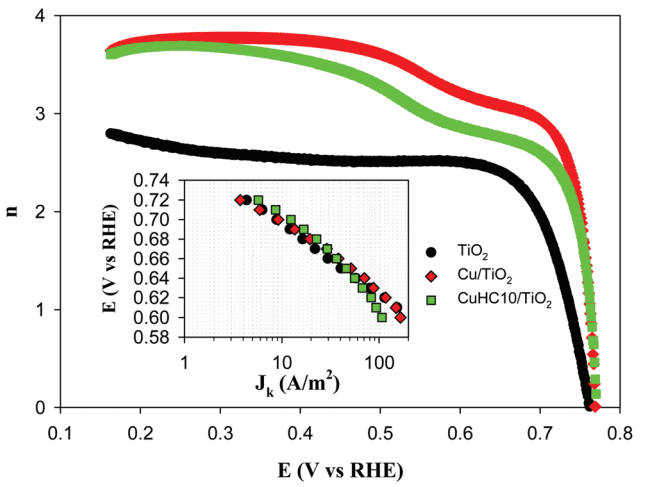

Fig. 6 Variation of the number of electrons transferred (n) in oxygen reduction with the electrode potential for TiO_2 (black curves), Cu/TiO_2 (red curves) and CuHC10/TiO_2 (green curves) nanoparticles. Symbols were experimental data calculated from the RRDE voltammograms at 1600 rpm in Fig. 5. The inset shows the corresponding Tafel plots. Data are acquired from linear regressions of the Koutecky–Levich plots in Fig. S2.† The electrode geometrical surface area was used to calculate the current density.

Further insight into the electron-transfer kinetics of oxygen reduction were revealed by Koutecky–Levich analysis, as the RRDE voltammetric currents include both kinetic (I_k) and diffusion (I_d) controlled contributions,[42]

$$\frac{1}{I_D} = \frac{1}{I_k} + \frac{1}{I_d} = \frac{1}{I_k} + \frac{1}{B\omega^{1/2}} \quad (1a)$$

$$B = 0.62nFAC_O D_O^{2/3} \nu^{-1/6} \quad (1b)$$

$$I_k = nAFkC_O \quad (1c)$$

where ω is the electrode rotation rate, n is the overall number of electrons transferred, F is Faraday's constant, C_O is the bulk concentration of O_2 dissolved in the electrolyte, D_O is the diffusion coefficient of O_2, and ν is the kinetic viscosity of the electrolyte.[43] Fig. S2† shows the Koutecky–Levich plots (I_D^{-1} *vs.* $\omega^{-1/2}$) of (A) TiO_2, (B) Cu/TiO_2 and (C) $CuHC10/TiO_2$ nanoparticles within the potential range of +0.76 to +0.60 V. One can see that all experimental data exhibited good linearity and the slopes of each nanoparticle catalyst remained approximately constant. The linearity and parallelism of the plots are usually taken as a strong indication of a first-order reaction with respect to dissolved oxygen. From the linear regressions in Fig. S2,† the kinetic currents (I_k) could also be quantified from the *y*-axis intercepts. This is manifested in the Tafel plot (inset of Fig. 6), where it can be seen that within the low overpotential region (E > +0.66 V), the kinetic currents increase in the order of TiO_2 < Cu/TiO_2 < $CuHC10/TiO_2$. For instance, at +0.70 V, the kinetic current density (J_k) was 8.83 A m^{-2} for TiO_2, 9.18 A m^{-2} for Cu/TiO_2 and 12.38 A m^{-2} for $CuHC10/TiO_2$, indicating that $CuHC10/TiO_2$ stood out as the best catalyst among the series (one may note that at high overpotentials (E < +0.66 V), the J_k values were actually higher for Cu/TiO_2 than for $CuHC10/TiO_2$. This may be ascribed to the much higher concentration of CuO in Cu/TiO_2 that was electrochemically reduced to Cu_2O at these potentials (Fig. 4) as Cu_2O was known to be active in ORR, *vide infra*).

The slope of the Tafel plot can also be used to gain further insight into the dynamics of the oxygen reduction reaction. For oxygen electroreduction at nanoparticle catalyst surfaces, the Tafel slopes are typically found at 60 mV dec^{-1} or 120 mV dec^{-1}, where the former corresponds to a pseudo two-electron reaction as the rate determining step, and in the latter, ORR is presumed to be limited by the first-electron reduction of oxygen.[44] In the present study, linear regressions of the Tafel plots yield a slope of 70.5 mV dec^{-1} for TiO_2, suggesting that the oxygen reduction reaction was largely limited by a pseudo two-electron process (corresponding to a relatively large fraction of peroxide species in the reduction products). For $CuHC10/TiO_2$, the Tafel plot actually includes two linear segments with different slopes. At low current densities (E > +0.66 V), the Tafel slope was about 58.5 mV dec^{-1}, implying the pseudo two-electron reaction as the rate-determining step in the low overpotential region. At high current densities (E < +0.66 V) the Tafel slope increased to 118.5 mV dec^{-1}, consistent with the first-electron reduction of oxygen as the rate-determining step (implying a facile O–O bond breaking step at high overpotentials). Similar behaviors can be seen with the Cu/TiO_2 sample with the two slopes of 56.7 mV dec^{-1} and 90.2 mV dec^{-1}, respectively. Dual Tafel slopes in ORR have been observed previously with Pt-based electrocatalysts,[45] and accounted for using a double-trap kinetic model,[46] where the turning point (+0.66 V in the present study) reflects the equilibrium potential for the dynamic transition between surface-adsorbed reaction intermediates like O* and HO*. Note that this potential coincided with the formation of Cu_2O for both $CuHC10/TiO_2$ and Cu/TiO_2, as shown in Fig. 4, and Cu_2O has been suggested to serve as effective active sites for ORR by donating electrons to oxygen.[19] Additional contributions may arise from the relatively hydrophilic surfaces of $CuHC10/TiO_2$ and Cu/TiO_2 hybrid nanoparticles that facilitated water dissociation and formation of surface-adsorbed hydroxyl species, as evidenced by XPS measurements (Fig. 3), where fast interactive effusion of H-adatoms over hydrated surfaces has been believed to enhance the electrocatalytic activity.[47,48] Furthermore, the Ti^{3+} defects in $CuHC10/TiO_2$ (Fig. 3) might also help enhance the adsorption and eventual reduction of oxygen on copper by interfacial charge transfer.[29] All these led to a much enhanced ORR activity of $CuHC10/TiO_2$ as compared to those of Cu/TiO_2 and TiO_2.

Durability is another important parameter in the evaluation of the nanoparticle catalytic performance. In the present study, durability tests were performed in oxygen-saturated 0.1 M NaOH at a potential sweep rate of 50 mV s^{-1} between +0.6 V and +1.1 V for 4000 cycles.[49] The RDE polarization curves before (solid curves) and after (dashed curves) durability tests are shown in Fig. 7. It can be seen that for TiO_2 nanoparticles alone (black curves), the polarization curve showed a cathodic shift of about 10 mV with virtually no change of the diffusion limiting current. For the Cu/TiO_2 nanoparticles (red curves),

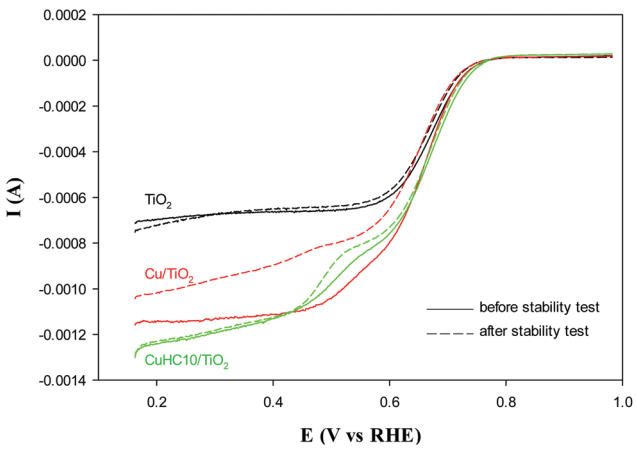

Fig. 7 Polarization curves for oxygen reduction catalyzed by TiO_2, Cu/TiO_2, and $CuHC10/TiO_2$ before (solid curves) and after (dashed curves) 4000 potential cycles with a potential scan rate of 50 mV s^{-1} from +0.6 to +1.1 V in an O_2 saturated 0.1 M NaOH solution. Electrode rotation rate: 1600 rpm. Other experimental conditions were the same as in Fig. 5.

the polarization curve was negatively shifted by as much as 30 mV, along with about 9% diminishment of the limiting current. In sharp contrast, no apparent change was observed with CuHC10/TiO_2 (green curves), indicating markedly enhanced stability of the hybrid nanoparticles that was likely due to the decyne capping ligands.

One may note that the electrocatalytic performance of these Cu/TiO_2 and CuHC10/TiO_2 hybrid nanoparticles remains subpar as compared to those of Pt or Pd-based nanoparticle catalysts which typically exhibit an onset potential more positive than +0.90 V and $n \approx 4.0$.[7,8,50,51] Yet, the activity is actually rather comparable to that of Au–TiO_2 nanocomposites (10–50 nm in diameter, n = 3.7 at +0.60 V, onset potential +0.88 V),[52] and markedly better than that observed previously with alkyne-capped copper nanoparticles.[19] In the latter, the nanoparticles (4–6 nm in diameter) were also capped with 1-decyne, and carbon black rather than TiO_2 nanoparticles was used as the catalytic support.[19] Without the strong metal–support interactions from TiO_2, however, peroxide species constituted a major portion of the oxygen reduction products (n = 2.5–2.7 within the potential range of +0.70 to +0.40 V) and the corresponding limiting current at 2500 rpm was only 0.8 mA. This signifies the importance of TiO_2 in the activation of water and the formation of surface adsorbed hydroxyl species for oxygen reduction in the so-called primary oxide spillover mechanism. It should be emphasized that the ORR activity of copper-based bulk electrodes is rather marginal.[16–18,53] For instance, in the previous studies with a polycrystalline Cu or CuNi electrode,[16,17] the onset potentials for oxygen reduction were found to be around +0.36 V (*vs.* RHE) in a borax buffer solution, and even more negative onset potentials were observed with single-crystalline Cu(100) and Cu(111) electrodes in H_2SO_4 at about 0 V (*vs.* RHE).[18,53] These are far more negative than those observed above with the hybrid nanoparticles.

4. Conclusion

In this study, copper nanoparticles with or without 1-decyne capping ligands were grown onto TiO_2 nanocolloid surfaces. The structures of the resulting nanocomposites were then subjected to a wide range of characterization methods. TEM measurements showed that the TiO_2 colloids were largely of anatase phase, and the close proximity of the TiO_2(101) and Cu(111) lattice fringes suggested intimate contact between the two components. Further structural details were unravelled by XRD measurements where the diffraction features of anatase TiO_2 were clearly defined whereas those of copper were not resolved, likely because of the small size and low loading of copper in the composites. XPS measurements suggested the formation of CuO in both hybrid nanoparticles, with a much higher concentration in Cu/TiO_2 than in CuHC10/TiO_2, most probably because of the decyne capping ligands in the latter. Interestingly, Ti^{3+} species were identified in CuHC10/TiO_2 nanoparticles but not in Cu/TiO_2, which may, at least in part, account for the enhanced ORR activity of the former. Electrochemical studies indicated that the electrocatalytic activity in oxygen reduction in alkaline media was significantly improved after copper species were chemically grown onto TiO_2 nanoparticles, as manifested by the increase in the number of electrons transferred from about 2.69 up to 3.74, an apparent anodic shift of the onset potential, a rather drastic increase of the kinetic current density and a remarkable long-term stability. Among the series, the best performance was observed with CuHC10 nanoparticles, which was ascribed to the activation of water by TiO_2 and the formation of surface-adsorbed hydroxyl species facilitated by defective Ti^{3+} sites. Taken together, the results presented herein indicate that the synergistic interactions between non-precious metals and metal oxides might be exploited for the development of effective catalysts based on earth-abundant and cost-effective materials for fuel cell electrochemistry.

Acknowledgements

This work was supported in part by the National Science Foundation (CHE-1012258, CHE-1265635, and DMR-1409396). TEM and XPS work was carried out at the National Center for Electron Microscopy and Molecular Foundry, Lawrence Berkeley National Laboratory as part of a user project.

Notes and references

1 E. Proietti, F. Jaouen, M. Lefèvre, N. Larouche, J. Tian, J. Herranz and J.-P. Dodelet, *Nat. Commun.*, 2011, **2**, 416.
2 F. T. Wagner, B. Lakshmanan and M. F. Mathias, *J. Phys. Chem. Lett.*, 2010, **1**, 2204–2219.
3 R. Rizo, E. Herrero and J. M. Feliu, *Phys. Chem. Chem. Phys.*, 2013, **15**, 15416–15425.
4 H. H. Wang, Z. Y. Zhou, Q. A. Yuan, N. Tian and S. G. Sun, *Chem. Commun.*, 2011, **47**, 3407–3409.
5 J. Zhang, K. Sasaki, E. Sutter and R. R. Adzic, *Science*, 2007, **315**, 220–222.
6 Z. Y. Zhou, X. W. Kang, Y. Song and S. W. Chen, *Chem. Commun.*, 2012, **48**, 3391–3393.
7 Z. Y. Zhou, X. W. Kang, Y. Song and S. W. Chen, *J. Phys. Chem. C*, 2012, **116**, 10592–10598.
8 K. Liu, X. W. Kang, Z. Y. Zhou, Y. Song, L. J. Lee, D. Tian and S. W. Chen, *J. Electroanal. Chem.*, 2013, **688**, 143–150.
9 R. Bashyam and P. Zelenay, *Nature*, 2006, **443**, 63–66.
10 M. Lefevre, E. Proietti, F. Jaouen and J. P. Dodelet, *Science*, 2009, **324**, 71–74.
11 G. Wu, K. L. More, C. M. Johnston and P. Zelenay, *Science*, 2011, **332**, 443–447.
12 S. Wang, D. Yu and L. Dai, *J. Am. Chem. Soc.*, 2011, **133**, 5182–5185.
13 S. Koh and P. Strasser, *J. Am. Chem. Soc.*, 2007, **129**, 12624–12625.

14 N. N. Kariuki, X. Wang, J. R. Mawdsley, M. S. Ferrandon, S. G. Niyogi, J. T. Vaughey and D. J. Myers, *Chem. Mater.*, 2010, **22**, 4144–4152.
15 H. H. Li, C. H. Cui, S. Zhao, H. B. Yao, M. R. Gao, F. J. Fan and S. H. Yu, *Adv. Energy Mater.*, 2012, **2**, 1182–1187.
16 M. V. Vazquez, S. R. Desanchez, E. J. Calvo and D. J. Schiffrin, *J. Electroanal. Chem.*, 1994, **374**, 189–197.
17 S. Cere, M. Vazquez, S. R. de Sanchez and D. J. Schiffrin, *J. Electroanal. Chem.*, 2001, **505**, 118–124.
18 T. Jiang and G. M. Brisard, *Electrochim. Acta*, 2007, **52**, 4487–4496.
19 Y. Song, K. Liu and S. W. Chen, *J. Power Sources*, 2014, **268**, 469–475.
20 T. J. Schmidt, H. A. Gasteiger, G. D. Stab, P. M. Urban, D. M. Kolb and R. J. Behm, *J. Electrochem. Soc.*, 1998, **145**, 2354–2358.
21 M. K. Min, J. H. Cho, K. W. Cho and H. Kim, *Electrochim. Acta*, 2000, **45**, 4211–4217.
22 N. Rajalakshmi, N. Lakshmi and K. Dhathathreyan, *Int. J. Hydrogen Energy*, 2008, **33**, 7521–7526.
23 B. E. Hayden, D. V. Malevich and D. Pletcher, *Electrochem. Commun.*, 2001, **3**, 395–399.
24 M. Wang, D. J. Guo and H. L. Li, *J. Solid State Chem.*, 2005, **178**, 1996–2000.
25 J. P. Shim, C.-R. Lee, H.-K. Lee, J.-S. Lee and E. J. Cairns, *J. Power Sources*, 2001, **102**, 172–177.
26 S. Shanmugam and A. Gedanken, *J. Phys. Chem. C*, 2009, **113**, 18707–18712.
27 S.-Y. Huang, P. Ganesan and B. N. Popov, *ACS Catal.*, 2012, **2**, 825–831.
28 M. M. Jaksic, G. A. Botton, G. D. Papakonstantinou, F. H. Nan and J. M. Jaksic, *J. Phys. Chem. C*, 2014, **118**, 8723–8746.
29 T. L. Thompson and J. T. Yates, *Chem. Rev.*, 2006, **106**, 4428–4453.
30 D. C. Pan, N. N. Zhao, Q. Wang, S. C. Jiang, X. L. Ji and L. J. An, *Adv. Mater.*, 2005, **17**, 1991–1995.
31 R. Ramanathan, M. R. Field, A. P. O'Mullane, P. M. Smooker, S. K. Bhargava and V. Bansal, *Nanoscale*, 2013, **5**, 2300–2306.
32 Q. Zhu, J. S. Qian, H. Pan, L. Tu and X. F. Zhou, *Nanotechnology*, 2011, 22.
33 T. Ghodselahi, M. A. Vesaghi, A. Shafiekhani, A. Baghizadeh and M. Lameii, *Appl. Surf. Sci.*, 2008, **255**, 2730–2734.
34 C. D. Wagner, W. M. Riggs, L. E. Davis, J. F. Moulder and G. E. Muilenberg, *Handbook of x-ray photoelectron spectroscopy: a reference book of standard data for use in x-ray photoelectron spectroscopy*, Perkin-Elmer Corp, Eden Prairie, Minn., 1979.
35 K. S. Kim, *J. Electron Spectrosc. Relat. Phenom.*, 1974, **3**, 217–226.
36 B. Erdem, R. A. Hunsicker, G. W. Simmons, E. D. Sudol, V. L. Dimonie and M. S. El-Aasser, *Langmuir*, 2001, **17**, 2664–2669.
37 S. Sodergren, H. Siegbahn, H. Rensmo, H. Lindstrom, A. Hagfeldt and S. E. Lindquist, *J. Phys. Chem. B*, 1997, **101**, 3087–3090.
38 M. Kunat, S. G. Girol, U. Burghaus and C. Woll, *J. Phys. Chem. B*, 2003, **107**, 14350–14356.
39 R. Schaub, P. Thostrup, N. Lopez, E. Lægsgaard, I. Stensgaard, J. Nørskov and F. Besenbacher, *Phys. Rev. Lett.*, 2001, 87.
40 A. J. Nozik and R. Memming, *J. Phys. Chem.*, 1996, **100**, 13061–13078.
41 S. M. A. Elhaleem and B. G. Ateya, *J. Electroanal. Chem.*, 1981, **117**, 309–319.
42 A. J. Bard and L. R. Faulkner, *Electrochemical methods: fundamentals and applications*, Wiley, New York, 2nd edn, 2001.
43 W. Chen, J. M. Kim, S. H. Sun and S. W. Chen, *J. Phys. Chem. C*, 2008, **112**, 3891–3898.
44 J. J. Zhang, *PEM fuel cell electrocatalysts and catalyst layers: fundamentals and applications*, Springer, London, 2008.
45 G. He, Y. Song, K. Liu, A. Walter, S. Chen and S. W. Chen, *ACS Catal.*, 2013, **3**, 831–838.
46 J. X. Wang, F. A. Uribe, T. E. Springer, J. L. Zhang and R. R. Adzic, *Faraday Discuss.*, 2008, **140**, 347–362.
47 J. M. Jaksic, G. D. Papakonstantinou, D. Labou, A. Siokou and M. M. Jaksic, *Adv. Phys. Chem.*, 2011, **2011**, 1–22.
48 J. M. Jaksic, G. D. Papakonstantinou, D. Labou, A. Siokou and M. M. Jaksic, in *New and future developments in catalysis: hybrid materials, composites, and organocatalysts*, ed. S. L. Suib, Elsevier, Amsterdam, 2013, pp. 175–212.
49 B. Lim, M. Jiang, P. H. C. Camargo, E. C. Cho, J. Tao, X. Lu, Y. Zhu and Y. Xia, *Science*, 2009, **324**, 1302–1305.
50 S. Maheswari, P. Sridhar and S. Pitchumani, *Electrochem. Commun.*, 2013, **26**, 97–100.
51 L. Zhang, L. Y. Wang, C. M. B. Holt, T. Navessin, K. Malek, M. H. Eikerling and D. Mitlin, *J. Phys. Chem. C*, 2010, **114**, 16463–16474.
52 C. Lin, Y. Song, L. Cao and S. W. Chen, *ACS Appl. Mater. Interfaces*, 2013, **5**, 13305–13311.
53 G. Brisard, N. Bertrand, P. N. Ross and N. M. Markovic, *J. Electroanal. Chem.*, 2000, **480**, 219–224.

